



HAL
open science

4D in situ monitoring of the setting of alpha plaster using synchrotron X-ray tomography with high spatial and temporal resolution

J. Seiller, T. Bonnal, J. Adrien, S. Meille, S. Tadier, E. Maire, A. Bonnin

► To cite this version:

J. Seiller, T. Bonnal, J. Adrien, S. Meille, S. Tadier, et al.. 4D in situ monitoring of the setting of alpha plaster using synchrotron X-ray tomography with high spatial and temporal resolution. *Construction and Building Materials*, 2021, 304, pp.124632. 10.1016/j.conbuildmat.2021.124632 . hal-03482914

HAL Id: hal-03482914

<https://hal.science/hal-03482914>

Submitted on 2 May 2022

HAL is a multi-disciplinary open access archive for the deposit and dissemination of scientific research documents, whether they are published or not. The documents may come from teaching and research institutions in France or abroad, or from public or private research centers.

L'archive ouverte pluridisciplinaire **HAL**, est destinée au dépôt et à la diffusion de documents scientifiques de niveau recherche, publiés ou non, émanant des établissements d'enseignement et de recherche français ou étrangers, des laboratoires publics ou privés.



Distributed under a Creative Commons Attribution - NonCommercial 4.0 International License

4D *In situ* monitoring of the setting of α plaster using synchrotron X-ray tomography with high spatial and temporal resolution

J. Seiller¹, T. Bonnal¹, J. Adrien¹, S. Meille^{1*}, S. Tadier¹, E. Maire¹, A. Bonin²

¹ Univ Lyon, INSA Lyon, UCBL, CNRS, MATEIS UMR5510, Bât. Blaise Pascal, 7 Avenue Jean Capelle, Villeurbanne, France

²Paul Scherrer Institut, 5232 PSI Villigen, Switzerland

*Corresponding author, sylvain.meille@insa-lyon.fr

Abstract

This paper is dedicated to the *in situ* follow up of the setting of an α plaster using synchrotron X-ray tomography, with a high spatial resolution, down to 0.3 μm (0.16 μm voxel size), and a high time resolution with a scan every 30 s. This combination of spatial and time resolution is amongst the best reported in the literature so far and is of particular interest for the study of moderately rapid transformation of the microstructure at a small scale. It enables to characterize both the dissolution of hemihydrate particles and the precipitation of gypsum crystals. A dissolution rate for the hemihydrate particles is determined, in good coherence with previous work on β plaster using lab X-ray tomograph. A thickening of gypsum crystals with hydration time is also noted. A quantitative analysis of hydration is performed through the calculation of a microstructural degree of reaction from the X-ray tomography volumes, after peak deconvolution of the gray value histogram at different hydration times.

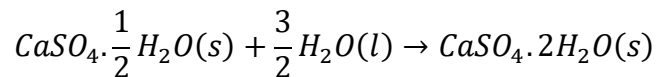
Keywords

Gypsum; calcium sulfate; hydration; *in situ* X-ray tomography; synchrotron

1. Introduction

Plaster, one of the most ancient construction material, is still frequently used today as plasterboard for buildings, making use of its lightness, good thermal insulation and fire resistance properties [1]. The plaster powder, or calcium sulfate hemihydrate ($\text{CaSO}_4, \frac{1}{2} \text{H}_2\text{O}$), is produced by calcination of gypsum, or calcium sulfate dihydrate ($\text{CaSO}_4, 2 \text{H}_2\text{O}$). Depending on the

production process, two types of hemihydrate exist: α and β . α hemihydrate is prepared by wet methods (autoclaving) whereas β hemihydrate is prepared by dry methods (calcination at 120-130°C) and this leads to crystals with a higher specific surface area. Those two hemihydrates differ by their reactivity with water, their microstructure and their mechanical strength in the set state. However they do not exhibit any difference in crystal structure [2]. Set plaster, or gypsum, is prepared by mixing the dry hemihydrate powder with water, leading to a hydration reaction as shown in the following equation:



The ratio of water to plaster powder (W/P) is a key parameter of the reaction. The stoichiometric ratio is equal to 0.186 but in order to increase the fluidity of the paste, the effective W/P ratio in industrial applications lies well above the stoichiometric value. The excess water turns into porosities after hydration and subsequent drying. The typical W/P ratio is between 0.3 and 0.4 for α hemihydrate, and between 0.7 and 0.8 for β hemihydrate, due to the higher water demand related to the higher specific surface area of the β hemihydrate crystals. This leads to approximately 25% and 50% of pores for α and β plaster, respectively. Gypsum samples prepared from α hemihydrate are therefore denser and harder than gypsum samples prepared from β hemihydrate. These are then dedicated to applications demanding higher mechanical properties. Gypsum is also often considered as a model material to study hydration reactions due to its high purity, its fully crystalline character and relatively simple chemistry.

The driving force for the hydration reaction of plaster is the difference in solubility of calcium sulfate hemihydrate and dihydrate, the former being more soluble in water than the latter at room temperature. Lavoisier was the first to describe this phenomenon in 1765 and since then, numbers of authors reviewed this reaction in literature [2,3]. Three stages can be identified in the hydration of plaster:

- dissolution of hemihydrate powder in water, forming a saturated ionic solution with respect to Ca^{2+} and SO_4^{2-} ,
- simultaneous nucleation and growth of gypsum crystals,
- final structuring of the set plaster by entanglement of gypsum needle-shaped crystals.

Various characterization methods are available to monitor the kinetics of the setting reaction, both in terms of chemistry (hydration reaction) and of mechanical properties [4]. The chemical degree of reaction can be monitored *in situ* through calorimetric methods [2], conductivity methods [5], X-ray powder diffraction [6], nuclear magnetic resonance [7], or FTIR spectrophotometry [8]. *Ex situ* methods, such as differential thermal analysis, are also available but they require to stop the reaction at different times. Therefore, one sample is needed per studied time.

Mechanical characterization can also be used to quantify the structuration of set plaster during the hydration reaction. The monitoring of the evolution of the elastic modulus versus time was for instance performed by the measurement of ultrasound speed of the setting paste in [9]. Lewry and Williamson followed the development of strength as the hemihydrate sets by three point bending test [10] and linked it with the evolution of the microstructure in a three steps model. First they observed the development of an interlocking matrix of gypsum crystal needles, resulting in an initial increase of the strength, immediately followed by a period of reduced strength due to release of internal stress as crystals grow against each other. Finally, an increase in strength was noted as a result of water evaporation during drying. This last stage illustrates the well-known sensitivity of the mechanical properties of set plaster to the presence of water [11][12].

As the crystalline entanglement controls the final strength of set plasters [13], a description of the development of the microstructure during the hydration reaction is of critical importance. Only few authors described the evolution of plaster microstructure during hydration. The work of Ridge, showing the growth of dihydrate needles by optical microscopy [14] was until recently the only study involving *in situ* monitoring of gypsum setting. Most of the studies were realized *ex situ*, requiring the reaction to be stopped at different times. Lewry and Williamson indeed monitored the setting reaction of hemihydrate by observing the microstructure using scanning electron microscopy (SEM) at different stages after stopping the hydration by ethanol washing [10]. They noted that dihydrate crystals had grown on partly solubilized hemihydrate particles during setting. SEM is widely used to study the local organization of crystals due to its high resolution. Recent work using liquid nitrogen quenching and subsequent sublimation of ice enabled the observation of plaster microstructure at early hydration times in an environmental SEM [15]. However, the use of SEM in the study of plaster hydration is limited as it is not suitable for an *in situ* monitoring. The protocol used to stop the hydration reaction, by ethanol washing of

liquid nitrogen quenching, may also have an impact on the microstructure. It has been shown that organic solvents in general, and ethanol in particular, help to inhibit the conversion from hemihydrate to dihydrate, as sought in such protocols. But using ethanol to stop the reaction may also dehydrate the already formed gypsum crystals, leading to porous hemihydrate particles, with the creation of voids resulting from the removal of water [16].

Thus, X-Ray tomography appears as a good candidate for the monitoring of plaster setting because it allows an *in situ* observation of the evolution of the 3D microstructure versus time, thus permitting to quantify it in 4 dimensions (3 spatial and one temporal dimensions). The first tomography scans of gypsum were acquired at high resolution using synchrotron source on a hydrated plaster [17]. In this study by Bentz et al., the simultaneous presence of both partially reacted hemihydrate particles and gypsum crystal needles in the reaction medium was shown. More recently, 3D scans with a voxel size of 3 μm of hydrating plaster were acquired after having stopped the reaction after 60 minutes [7]. Pore distribution was analyzed but no description of the microstructure evolution with setting of the plaster was made.

The only study involving an *in situ* monitoring of plaster setting using X-ray tomography is the work by Adrien [18] in which an industrial β plaster hydration was followed with a voxel size of 2.5 μm using a laboratory tomograph with acquisition time of about 3 minutes per scan. Both qualitative and quantitative observations were carried out. Size of the initial hemihydrate particles was shown to play a critical role on the rate of dissolution and on the final microstructure as largest particles led to formation of mesopores. Monitoring such a process requires that a compromise is reached between acquisition time and spatial resolution. At moderate resolution (3 μm), many studies have reported acquisition times down to 1 Hz [19,20]. At higher resolution (on the order of 100 nm voxel size), the fastest acquisition time reported so far is the study by Villanova et al [21], down to 10 seconds per scans but with a strong content of phase contrast in the radiographs.

In this study, the setting of α plaster is followed by X-Ray tomography acquisitions achieved at a synchrotron X-ray source. Compared to conventional X-ray sources, synchrotrons have higher brilliance and higher beam coherence. Those properties give the possibility to work with monochromatic beam at high flux and high resolution. Furthermore, when X-rays travel through materials with different refractive indices, interference phenomena occur. By increasing the distance between the sample and the detector, the contrast between the different components

of the material can be enhanced. The use of synchrotron phase contrast X-ray imaging permits in the present work to reduce the voxel size down to $0.163\ \mu\text{m}$ and to lower the exposure time down to 30 or 40 seconds, which is of interest for the capture of quick processes like the studied hydration reaction [22,23]. Both qualitative and quantitative analyses of the 3D volumes are reported. The dissolution kinetics of hemihydrate particles is studied, as well as precipitation of gypsum crystals.

2. Materials and method

2.1. Characterization of the hemihydrate powder

An α calcium sulfate hemihydrate was kindly supplied by Saint-Gobain with a purity above 99%. The main impurity is calcium carbonate.

Figure 1.a displays the particle size distribution of the hemihydrate (HH) powder, first maintained 24 h at 45°C , then measured by laser diffraction granulometry using a dry powder dispersion unit (Malvern Mastersizer with a Scirocco 2000 unit, Malvern Panalytical, UK). The particle refractive index was set to 1.525, the particle absorbance index to 0.1 and the measurement was repeated for four different batches of HH powder. Additionally, the HH powder was gold coated and observed with a Philips XL20 Scanning Electron Microscope (SEM) using secondary electrons imaging, as shown in Figure 1.b. The micrograph reveals large hemihydrate particles (smallest dimension $> 10\ \mu\text{m}$) covered by tiny and irregular particles ($< 1\ \mu\text{m}$). Consistently with their particle size distribution, HH particles of intermediate sizes (dimensions approaching $5\ \mu\text{m}$) could also be observed. Thus, the particles composing the HH powder were sorted out in three different classes:

- 1st class of particles with mean sizes inferior to one micron (peak centered at $0.6\ \mu\text{m}$ in Figure 1.a).
- 2nd second class with mean sizes of a few microns (peak centered at $4.4\ \mu\text{m}$).
- 3rd class corresponding to the biggest particles with sizes of several tenths of microns (peak centered at $26.3\ \mu\text{m}$).

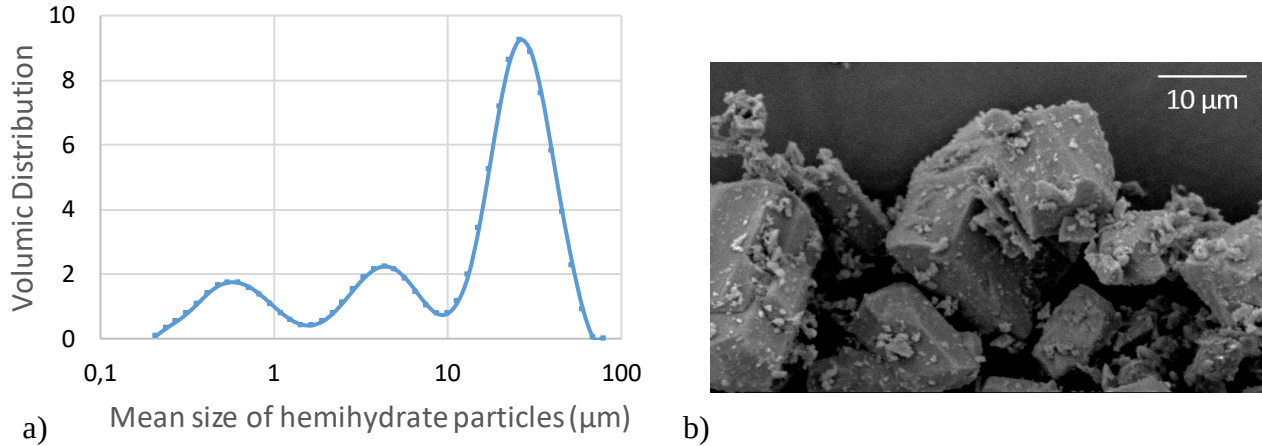


Figure 1: a) Particle size distribution in volume of the hemihydrate powder ($n = 4$). The plot represents the mean value of four measurements performed on different batches. b) SEM micrograph of the hemihydrate powder.

2.2. α -plaster preparation

The reactive powder was stored in a drying oven at 45°C for one night and then mixed with tap water with a W/P weight ratio of 0.4. Powder and water were hand-mixed for 30 s, then left at rest for 30 s and finally hand-mixed for an additional 30 s.

For an *in situ* observation of the setting with synchrotron X-Ray tomography, the paste was injected with a syringe into a drinking straw of inner diameter 1 mm and thickness 0.25 mm mounted on the rotation stage of the synchrotron beamline. The voxel size was 0.163 or 0.65 μm depending on the optics used, and the total lateral sizes of the field of view were around 300 μm and 1.2 mm, respectively. The time when the hemihydrate powder was put in contact with the water is referred hereafter as the initial time of the monitoring ($t = 0$). The time when the paste was injected in the straw was 144 s and 148 s for the 0.65 μm and the 0.163 μm voxel size acquisitions respectively. Setting time was evaluated in parallel using the extra-paste that was not injected in the straw with the knife setting time method. In this method, the setting time corresponds to the time after which a cut made in the paste with a blade remains open.

2.3. X-ray tomography – *In situ* setting of the plaster

The observation of the microstructure evolution during the setting was carried out by means of X-Ray tomography operated at the TOMCAT beamline of the Swiss Light Source (SLS) at the Paul Scherrer Institute in Villigen, Switzerland. Ambient temperature was $22 \pm 2^\circ\text{C}$.

The samples were scanned with a monochromatic X-ray beam at an energy of 20 keV. This value of 20 keV provides the most efficient photon flux (higher photon counts in a given counting time) collected by the detector system used in this study. This value is commonly used in materials science and engineering. It remains sufficiently low to provide a lot of contrast and sufficiently high to provide enough transmission across absorbent samples like plaster. X-rays were converted in visible light through a LSO:Tb 5.9 μm thick scintillator and detected by a 2560 x 2160 pixels sCMOS camera (PCO Edge 5.5) at a distance of 10 mm from the sample. This distance was chosen as a trade-off to provide enough phase contrast and thus increase the contrast compared to attenuation only. This distance cannot be increased too much however especially in the case of plaster to reduce the scattering and multiple fringes effect in such a complex microstructure. Using the subsequent phase retrieval with the Paganin algorithm as we did usually provide a reconstruction with little artifacts and excellent sharpness. The most appropriate ratio Δ/β used during phase retrieval was chosen by trial and error and by comparing the Paganin reconstruction and the standard reconstruction (with no phase retrieval). The best image quality was obtained with $\Delta/\beta = 10$. The employed ratio was the same for all the reconstructions.

The projection images were magnified 10 or 40 times, resulting in voxels size of 0.65 μm and 0.163 μm respectively. There was no exact measurement of the actual physical resolution of the detecting chain before or after this experiment. For this reason, we will only speak about “voxel size” in this paper. It is known however that depending on many experimental parameters related to the beam, the tomograph and/or the sample itself (Signal to Noise Ratio, partial volume effect, etc...), the actual resolution can be up to 4 times larger than the voxel size. Provided the quality of the optics used in the present study and sharpness of the reconstructed images, we rather believe that in our case, the resolution is closer to 2 times the voxel size. It was sometimes possible to acquire the scan of a same sample at a given location at the two available resolutions but this was not attempted during the *in situ* analysis. For the acquisition, a continuous rotation was chosen with an integration time of 50 ms (at 0.65 μm) and 80 ms (at 0.163 μm) for each of the 600 projections acquired over a sample rotation of 180°. Therefore a complete scan lasted 30 and 40 seconds respectively. Note that this combination of rather high spatial and temporal resolution is not frequent in materials science.

For the experiment with a voxel size of 0.65 μm , the first scan was acquired at 499 s (8 min 19 s) after the initial time, corresponding to the time required to prepare the sample and the time

for the first acquisition. In total, 16 acquisitions were performed until 8600 s (approx. 2 h 24 min) after the initial time. To optimize the monitoring of the setting without collecting too many data, time intervals between two successive acquisitions were progressively extended as the reaction proceeded: the time interval was as short as possible at the beginning of the process (100 s) and then longer (> 3000 s between the 15th and the 16th scans). For the experiment with a voxel size of 0.163 μm , the first scan was acquired at 460 s (7 min 40 s) after the initial time, and 22 acquisitions were performed until 8325 s (approx. 2 h 20 min) after the initial time. After that, no more change in the microstructure could be detected.

After drying of the samples for a day at 45°C, a final scan was carried out at the same voxel sizes (0.163 and 0.65 μm). Improved conditions were chosen for the sample scanned at a voxel size of 0.163 μm : the number of projections was increased to 1000. After scan acquisition, a phase retrieval algorithm was applied [24] on the projections to increase the contrast and reduce the noise. Volumes were then reconstructed from the projections using the Gridrec algorithm [25]. The gray value of each voxel, linked to the material specific X-ray attenuation coefficient, is normalized to 16 bit gray values. Therefore, the voxel gray values are not directly representative of the attenuation coefficient.

2.4. Volume analysis and quantification

The public domain ImageJ/Fiji shareware [26][27] was used for image processing and visualization. The reconstructed volumes were first spatially registered (each scan was geometrically aligned with respect to the previous one) as during setting, the sample can drift. After a 3D median filtering, 3D images were cropped in order to obtain a suitable size for observation and quantification.

On the scan with a voxel size of 0.65 μm , the total analyzed volume was of (240 μm)³. This volume was considered sufficient to be representative of the whole sample and was used for the global 3D quantification of the microstructure versus time. To estimate the volume fractions and for 3D rendering purposes, the different phases present in the setting paste (i.e. entrapped air, hemihydrate and gypsum crystals and ionic solution) were distinguished by multiple thresholding.

The evolution of the microstructure during setting was studied at a global scale by the evolution of voxel gray value histograms from 499 s to 8600 s and also at a local scale by the follow-up of individual particles after thresholding.

Evolution at a global scale: gray values histograms

As for the histograms, each single phase present in the setting paste should theoretically be identified by one specific gray value. However, due to classical quantic noise and to the spatial resolution of the technique leading to partial volume effect and a partial overlap of the peaks in the gray value histogram was observed. Therefore, a peak deconvolution was performed to quantify the contribution of each of the three phases, considering a Gaussian distribution of their gray values. Histograms were thus fitted with a combination of three Gaussian distributions:

$$\sum_{i=1}^3 I_i \cdot N_i(\mu_i, \sigma_i)$$

with I_i the intensity applied to the normal distribution N_i of mean μ_i and of variance σ_i^2 .

To avoid non-physical results, constraints were applied during the fitting process: intensities of the Gaussians had to be positive: $I_i > 0$, mean values had to be in the gray level range $\mu_i \in [0,64000]$ and standard deviations were limited to $\sigma_i = 10000$.

In a second step, the histograms were used to evaluate the relative volume fractions of each phase. Firstly, each peak was normalized using a Euclidean norm: the result S_i is considered close to the hypothetical histogram, which could be obtain if each phase was scanned alone. Secondly, a linear law of mixture was considered to evaluate the volume fractions c_i . Thus, working on normalized histograms H_i :

$$H_i = \sum_{i=1}^3 c_i \cdot S_i$$

As in the first step, constraints have been applied for the determination of c_i . The relative volume fractions have been considered positive: $c_i > 0$ and the absorption of X-rays has been considered arising only from the three phases: $\sum_i c_i = 1$.

Evolution at a local scale: follow-up of individual particles

Concerning the monitoring of individual particles, 100 hemihydrate particles of various initial sizes were selected manually to study their dissolution kinetics. They were sorted into five classes depending on their size and their size evolution was monitored versus time. For each class, the average local thickness was calculated. The local thickness is defined as the diameter of the

largest sphere that fits inside the object. It can therefore be considered as the smallest lateral dimension of the object. Note that for longer reaction times, the precipitation of gypsum crystals hampers the use of this method as hemihydrate particles and gypsum crystals become difficult to distinguish. Therefore, after binarization of the volume, a cycle of 4 erosions followed by 4 dilatations was applied in order to eliminate the smallest crystals so that they were not taken into account in the thickness measurement. The smallest particles (with thicknesses smaller than 10 voxels, i.e., 6.5 μm) could not be characterized due to the limited spatial resolution of these 3D images.

In the scans with a voxel size of 0.163 μm , 22 particles (smaller than 15 μm in thickness) were chosen and their thickness evolution was studied during time. To observe the precipitation of gypsum, gray level profiles of isolated dihydrate crystals were plotted versus time. A total of seven isolated growing gypsum crystals were selected and their thickness monitored versus time. Finally, a 3D render of these crystals was also computed.

3. Results

3.1. *In situ* qualitative observation of microstructural changes during setting

Figure 2 presents a same section of a reconstructed volume (0.65 μm voxel size) at six different times during the setting of the plaster. On the top left picture, corresponding to the first acquisition at 499 s after the initial time, hemihydrate particles of size ranging from a few micrometers to tens of micrometers can be observed in light gray. They are surrounded by a darker gray phase consisting of ionic solution and gypsum crystals nuclei (not visible). Some gypsum crystals can be imaged in the form of very thin needles (see red circle in the image at 499 s).

The evolution of the microstructure versus hydration time can be described as follows:

- a gradual dissolution of hemihydrate particles is observed, the smaller particles being the first to dissolve completely,
- the formation of a network of gypsum crystal needles can also be observed, initiated in the ionic solution.

Those two phenomena are concomitant, thus confirming a transport of matter from the dissolving hemihydrate particles to the crystallizing gypsum.

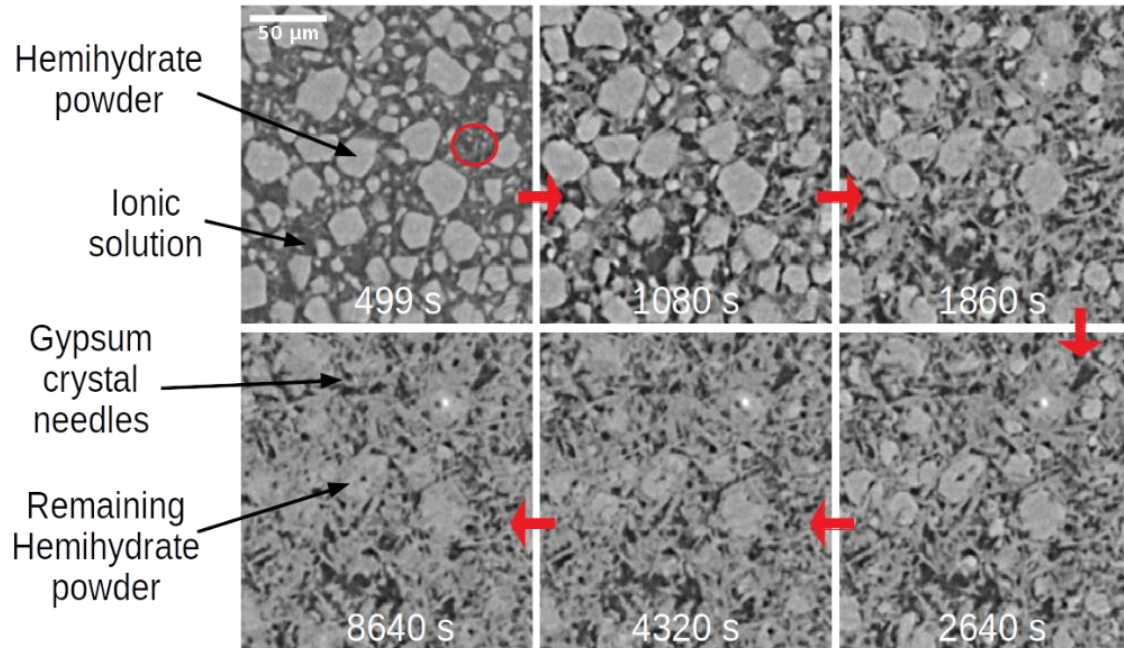


Figure 2: Microstructural changes during the setting of plaster. Evolution versus time of one same reconstructed 2D slice extracted from the 3D volumes acquired during the in situ tomography experiments with a voxel size of $0.65 \mu\text{m}$, between 499 and 8640 s.

The gray values of the hemihydrate particles being almost the same as those of gypsum crystals, it is difficult to distinguish the formers from the latters. However, it can be observed that even at long setting times, the biggest hemihydrate particles remain entrapped between gypsum crystals and do not dissolve completely. Moreover, after 4320 s (i.e. 72 min), no significant change in the microstructure could be observed anymore. This seems related to the rapid shortage of water during this experiment.

To have a finer description of the microstructural changes at small scale during setting, sections of the volume at $0.163 \mu\text{m}$ voxel size acquired at different setting times were also reconstructed (Figure 3). The simultaneous dissolution of hemihydrate particles and precipitation of gypsum crystals in the ionic solution is confirmed. However in this volume, even the biggest hemihydrate particles seem to be completely dissolved from a time of 4725 s (i.e. ≈ 79 min), contrarily to what is observed on the volume with $0.65 \mu\text{m}$ voxel size. It has to be noted that the largest particles in this volume are typically $15 \mu\text{m}$ thick as compared to $50 \mu\text{m}$ in the volume at a lower resolution. In the image at 8325 s (i.e. ≈ 140 min), two types of pores could be observed:

- Mesopores of about 10 microns in thickness (see circle on the image at 8325 s in Figure 3), left by the dissolution of some initially large hemihydrate particles. However, in other cases, the dissolution of some of the biggest hemihydrate particles led to the formation of an entanglement of crystal needles and not to a mesopore.
- Micropores in the form of an interconnected network between the entangled gypsum crystals.

In the analyzed volumes, no air bubble could be observed in the microstructure even if a few entrapped air bubbles are detected when the total volume of the sample is considered, as commonly encountered in set plaster.

The scanning resolution is high enough to image growing gypsum crystals and to monitor the evolution of their morphology with the hydration time. In Figure 4, the top line shows a growing gypsum crystal during hydration. The crystal appears in the image at 1180 s (i.e. ≈ 20 min) in the shape of a thin needle with a length of about 15 μm . It then progressively thickens with hydration time. Figure 4 (bottom line) shows the 3D rendering of the gypsum crystal versus time, after binarization. These images suggest that this crystal is not needle-shaped in reality but more lamella-shaped with a growing thickness as shown in Figure 4 (top line). During setting, the crystal grows first as a platelet in two directions, forming a very thin lamellae of dihydrate, and then thickens during time.

SEM micrographs of a fully hydrated sample confirm the observations made with X-ray tomography. The micrograph in Figure 12 reveals a network of gypsum crystals, with different shapes, either sharp needles of length ranging from 10 to 15 μm or lamellae of width ranging from 15 to 20 μm .

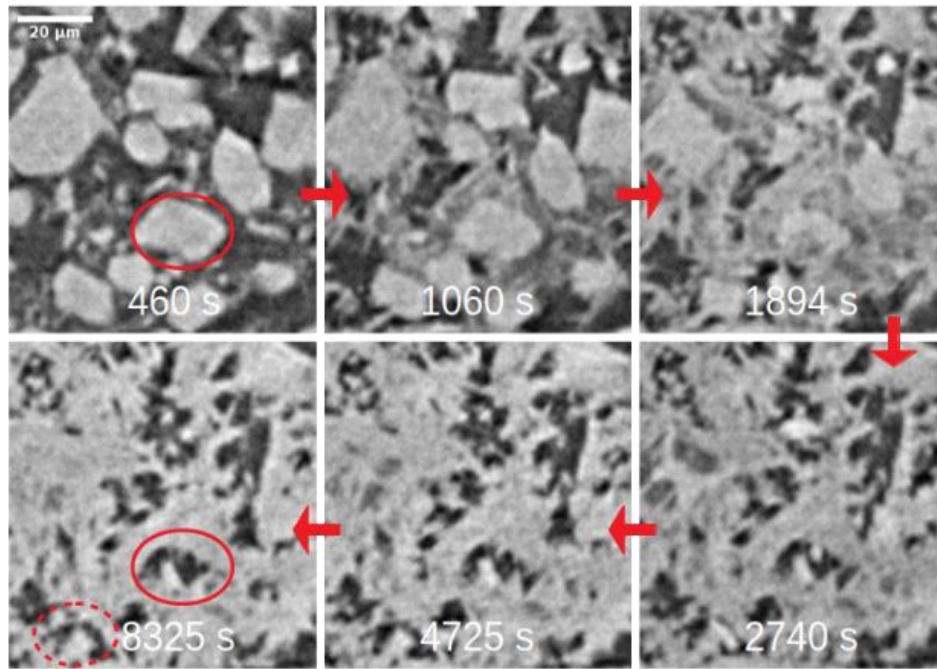


Figure 3: Microstructural changes during the setting of plaster. Evolution versus time of one same reconstructed 2D slice extracted from the 3D volumes acquired during the in situ tomography experiments with a voxel size of $0.163 \mu\text{m}$, between 460 and 8325 s. The red circles show a mesopore formed after dissolution of a hemihydrate particle. The dotted red circles show an initial hemihydrate particle and the same area after dissolution showing entangled crystals.

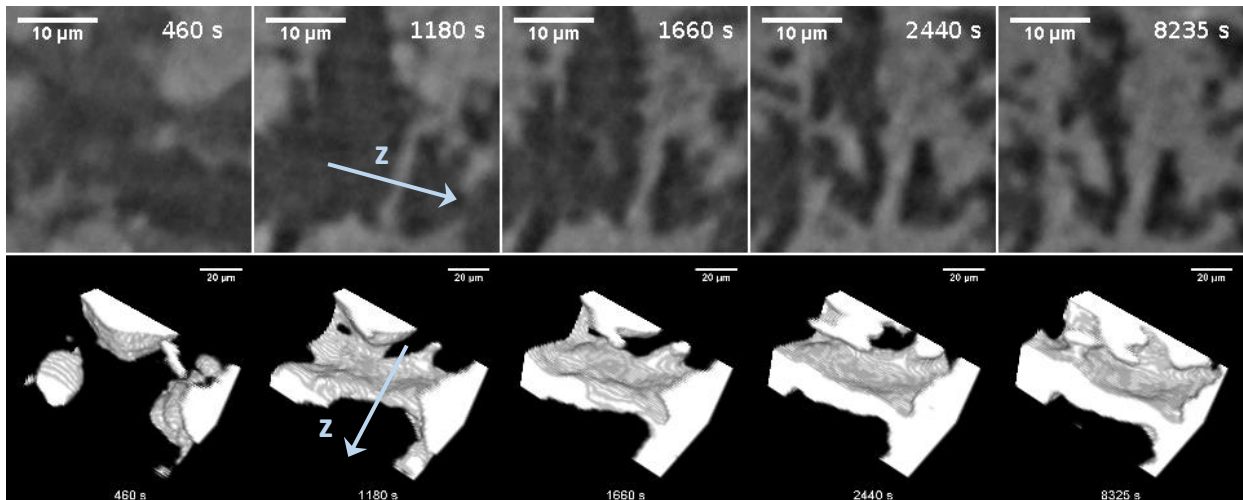


Figure 4: Illustration of the growth of a gypsum crystal. Evolution versus time of one same reconstructed 2D slice extracted from the 3D volumes acquired during the in situ tomography experiments with a voxel size of $0.163 \mu\text{m}$, between 460 and 8325 s (top line) and associated 3D visualization (bottom line).

3.2. In situ quantitative analysis

Quantification of porosity

The images with a 0.65 μm voxel size were used for this quantification because they are sufficiently resolved to reduce the partial volume effect and they encompass a larger portion of the material.

Final porosity in the set plaster is assessed by binarization of the reconstructed volume with 0.65 μm voxel size. Table 1 summarizes the level of porosity reached in the fully hydrated sample after drying for 24 hours. To illustrate the influence of the choice of the binarization threshold on the calculated porosity fraction, 3 different threshold values were selected. By visual observation, all three thresholds seem to correctly separate porosity and solid phase (see Figure 5) but the calculated porosity fraction shows a significant difference in terms of volume fraction.

Assuming that all H_2O molecules that do not participate to the hydration reaction will eventually dry and lead to pores, the theoretical porosity fraction of a pure α plaster fully hydrated with a W/P ratio of 0.4 is equal to 29.5%. The porosity fraction determined with the first threshold value appears to be relatively low, whereas the porosity fractions determined with thresholds 2 and 3 are closer to the theoretical value. Furthermore, it should be taken into account that the setting reaction of the plaster may not be fully completed here. Indeed, even at long reaction time as in the final scan, not totally dissolved hemihydrate particles can still be spotted (Figure 2). This can also lead to a slight underestimation of the porosity fraction.

Table 1: Final porosity computed from binarized images with different thresholds, as illustrated in Figure 5 after complete hydration and subsequent drying

	Threshold 1	Threshold 2	Threshold 3	Theoretical
16 bits gray value set as threshold value	25700	28270	30583	-
Total porosity fraction (%) calculated in the volume	22.5	27.6	33.1	29.5

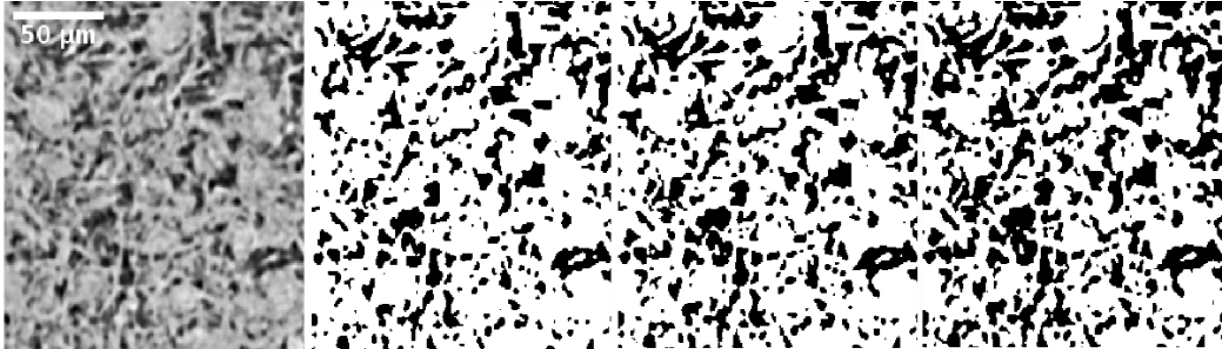


Figure 5: Section of a volume at $0.65 \mu\text{m}$ per voxel of entangled gypsum crystals. Same image before (left) and after binarization with different thresholds, i.e. a 16-bit gray value of 25700, 28270, and 30583 respectively (see Table 1)

Microstructural degree of reaction

As each phase present in the microstructure (air, ionic solution, hemihydrate and gypsum crystals) is characterized by a distinct gray value, the setting of plaster was followed through the computation of histograms of gray values distribution for the whole volume at each time.

At the time at which the acquisition was launched (~ 500 s), two peaks can be observed in the histogram, corresponding to the hemihydrate particles and to the ionic solution (see Figure 2 and Figure 3). Gypsum possibly exists in the form of small crystals that cannot be visualized yet. During setting, those two peaks merge in a single one corresponding to gypsum crystals.

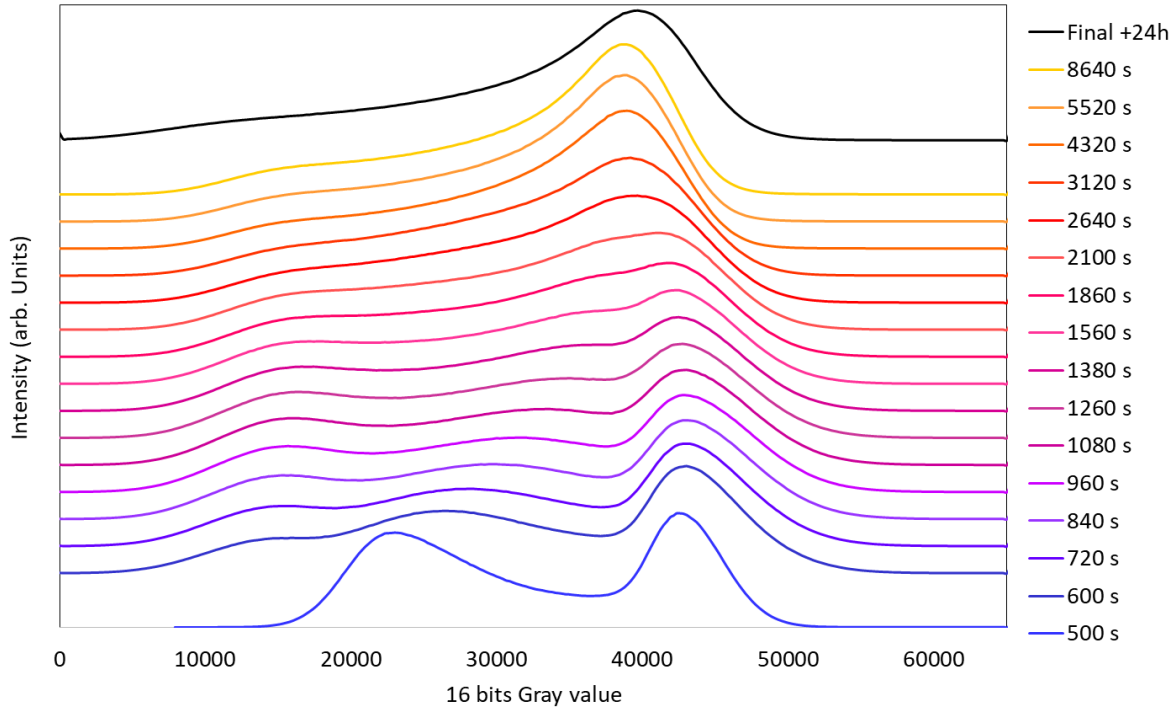


Figure 6: Histograms of the relative attenuation measured in the volumes for different times during setting and then subsequent drying at 45 °C.

The gray level histograms can be used to estimate the respective quantities of each phase during setting. As illustrated in Figure 6, the peaks corresponding to the interstitial water, possibly including gypsum nuclei (lowest gray values), gypsum crystals (intermediate gray values) and hemihydrate crystals (highest gray values) partially overlap and peak deconvolution appears to be necessary to quantify the contribution of each phase.

Figure 7a illustrates histograms for three different time points. The mean gray value for each phase is found nearly constant for the different time points: only a limited shift is noted for the peak corresponding to gypsum. This can be explained by the small size of the crystals as compared to the voxel dimension ($0.65 \mu\text{m}$ per voxel), especially at initial times. The characteristic mean value has been chosen at time 720 s for water and hemihydrate and at time 8640 s for gypsum. This choice is based on the fact that the characteristic gray value can be determined with a better accuracy in the presence of large volumes made of only one constituent in the whole material. Values obtained from acquisitions before 720 s and after 24h are not taken into account because the fitting with three Gaussian distributions is not satisfying for these times. The characteristics values for each peak are gathered in Table 2.

The volume fraction of each phase versus hydration time is plotted in Figure 7b. It shows a global decrease in the amount of hemihydrate and a respective increase of gypsum volume fraction with hydration time. A non-completed hydration is noted with a remaining hemihydrate fraction for the longest hydration times. The amount of interstitial water is shown to decrease with a small increase noted at the initial phase of hydration, up to 1000 s. This can be related to the dissolution of hemihydrate particles and to the precipitation of gypsum crystals too small to be identified with the voxel resolution used, and therefore counted as interstitial water. Figure 8b can be used to compute a microstructural degree of reaction from X-ray tomography. The knife setting time was 425 s (7 min 05 s) and 408 s (6 min 48 s) for the samples corresponding to the 0.65 μm and 0.163 μm voxel size respectively. This time corresponds to a relatively low volume fraction of gypsum precipitation (below 30%).

Table 2: Parameters of the Gaussians associated to water, gypsum and hemihydrate

	Intensity	Mean μ	Standard Deviation σ
Gaussian peaks	[count]	[Gray level - 24 bits -]	
n°1 (interstitial water)	0.047	14136	3031
n°2 (gypsum crystals)	0.075	33102	3666
n°3 (hemihydrate crystals)	0.135	43885	2599

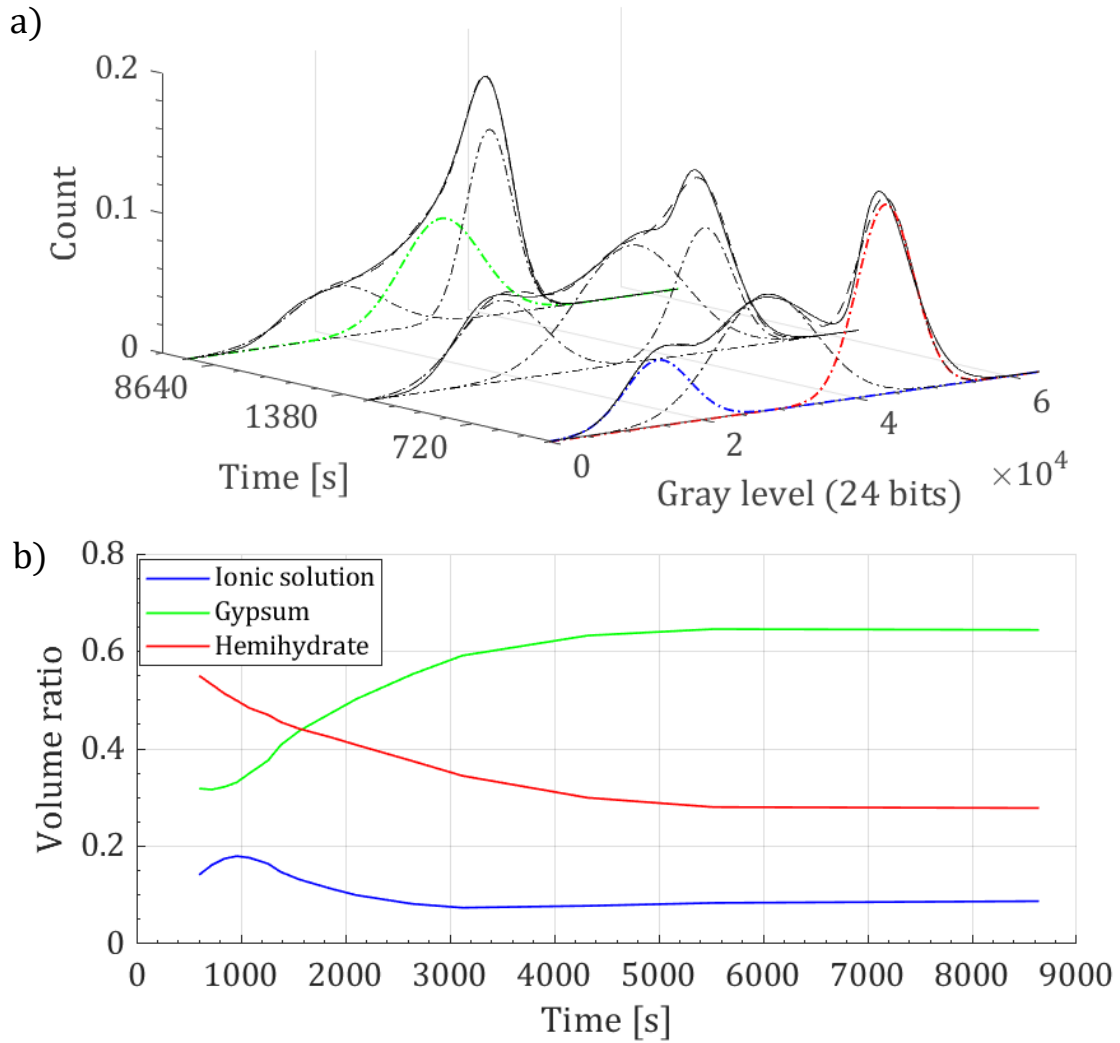


Figure 7: a) Plot of the gray values histograms for three different hydration times (720 s, 1380 s and 8640 s) with the peaks associated to the different phases composing the evolving paste. Peaks displayed in color were used to estimate the values given in Table 2; b) evolution of the respective volume fraction of the phases versus hydration time calculated for all acquisition times and starting at 600 s.

Hemihydrate particles dissolution kinetics

Figure 8.a presents the evolution of the mean thickness of 100 different hemihydrate particles, separated into 5 thickness classes, versus hydration time. It confirms that the biggest particles (with a size greater than 15 μm) are not dissolved completely as their final thicknesses do not reach zero. After approximately 3000 s, no more evolution of the hemihydrate thickness is noted, probably due to a shortage of water. It then appears that the dissolution of the hemihydrate starts from the liquid/solid interface. The dissolution speed is similar for each particle size but the

smallest particles are fully dissolved while the largest ones stop dissolving when water shortage occurs.

In order to compare the dissolution kinetics of different initial sizes of hemihydrate particles, the dissolution curves are normalized to their initial thickness value at 499 s. The evolution of T/T_{499} - thickness of the particle at a given time to its thickness at 499 s - is plotted on Figure 8.b. It appears that the incubation time (time before which no thickness decrease is noted) is constant for all particle sizes, around 800 s. The particles then dissolve completely for small particles, and stops for the largest particles after approximately 2000 s without reaching a complete dissolution.

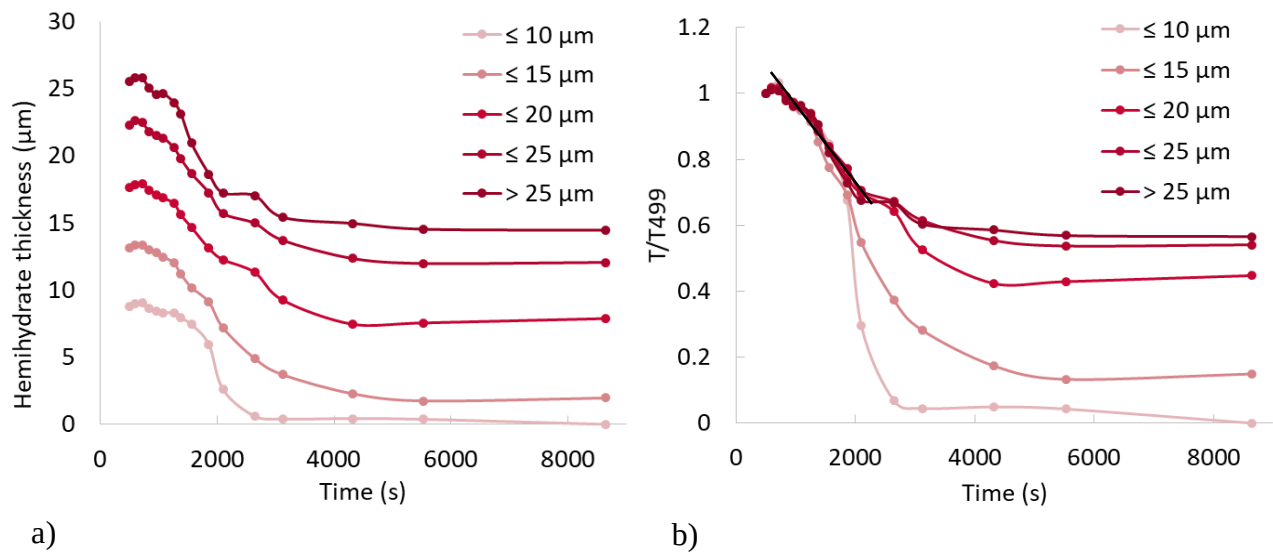


Figure 8: a) Hemihydrate thickness evolution during setting for different classes of initial particle thicknesses b) Normalized thickness evolution of hemihydrate particles. Measurements based on an average of 22 particles per size class.

As the spatial resolution of the volume with a voxel size of $0.65 \mu\text{m}$ is not sufficient to characterize precisely the smallest particles, a similar analysis was conducted on the reconstructed volumes with a voxel size of $0.163 \mu\text{m}$. The data were computed for 22 selected particles of hemihydrate with an initial thickness inferior to $15 \mu\text{m}$ (Figure 9). The curves are similar to those displayed in Figure 8, showing a first time-period with a limited dissolution speed, followed by a strong increase of dissolution rate, until complete dissolution of the particle. Moreover, it appears that the biggest particles needed more time to dissolve completely.

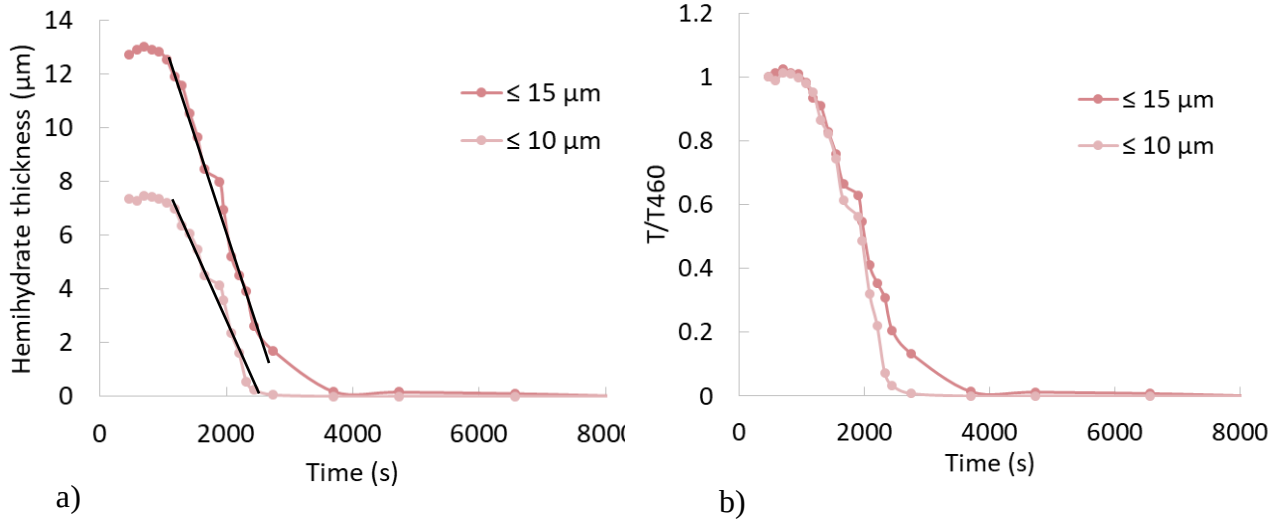


Figure 9: a) Hemihydrate thickness evolution during setting for two classes of smallest initial particle sizes b) Normalized thickness evolution versus time.

The dissolution rate of hemihydrate particles can be computed using the slope of the thickness of particles versus hydration time curve in the region of maximum dissolution (Figure 9.a). As the dissolution clearly starts from the solid liquid interface, it is quantified as the speed of motion of this interface and so they are calculated as the change of half-thickness versus time ($dT/2dt$) and are summarized in Table 3. Dissolution rates are found to be around $0.2 \mu\text{m}\cdot\text{min}^{-1}$. The main conclusion of the present measurement is that in the case of alpha plaster, the dissolution starts at the same time for all the particles regardless their size and the dissolution speed doesn't depend on the particle size. This is slightly different than our previous findings on beta plaster [18] where the dissolution starting time increased with the particle size.

Table 3: Dissolution rate of hemihydrate particles in the steady state regime for two different granulometric classes, calculation from volumes at $0.163 \mu\text{m}$ and $0.65 \mu\text{m}$ per voxel

Voxel size	0.163 μm		0.65 μm			
	≤ 10	≤ 15	≤ 15	≤ 20	≤ 25	> 25
Initial hemihydrate thickness (μm)						
$dT/2dt$ in the steady state ($\mu\text{m}/\text{min}$)	0.17	0.22	0.12	0.13	0.14	0.19

Kinetics of gypsum crystal growth

The precipitation and growth of gypsum crystals was monitored in two ways: first, a single growing crystal was isolated and the evolution of the gray value profile across the thickness of that crystal was plotted versus hydration time (Figure 10). At 460 s (very beginning of the setting), the profile shows a steady gray value corresponding to the ionic solution. With time, the gray value between 1 and 4 μm along the profile kept increasing with the precipitation of the gypsum crystal. An increase of crystal thickness can be noticed with increasing hydration time. Jointly, a decrease of the gray value can be noticed between 0 and 1 μm and between 4 and 5 μm , in the area surrounding the gypsum crystal. It can be noted that the gray value of interstitial water surrounding the growing gypsum crystal decreases with the thickening of the crystal. This can be related to a phase contrast effect.

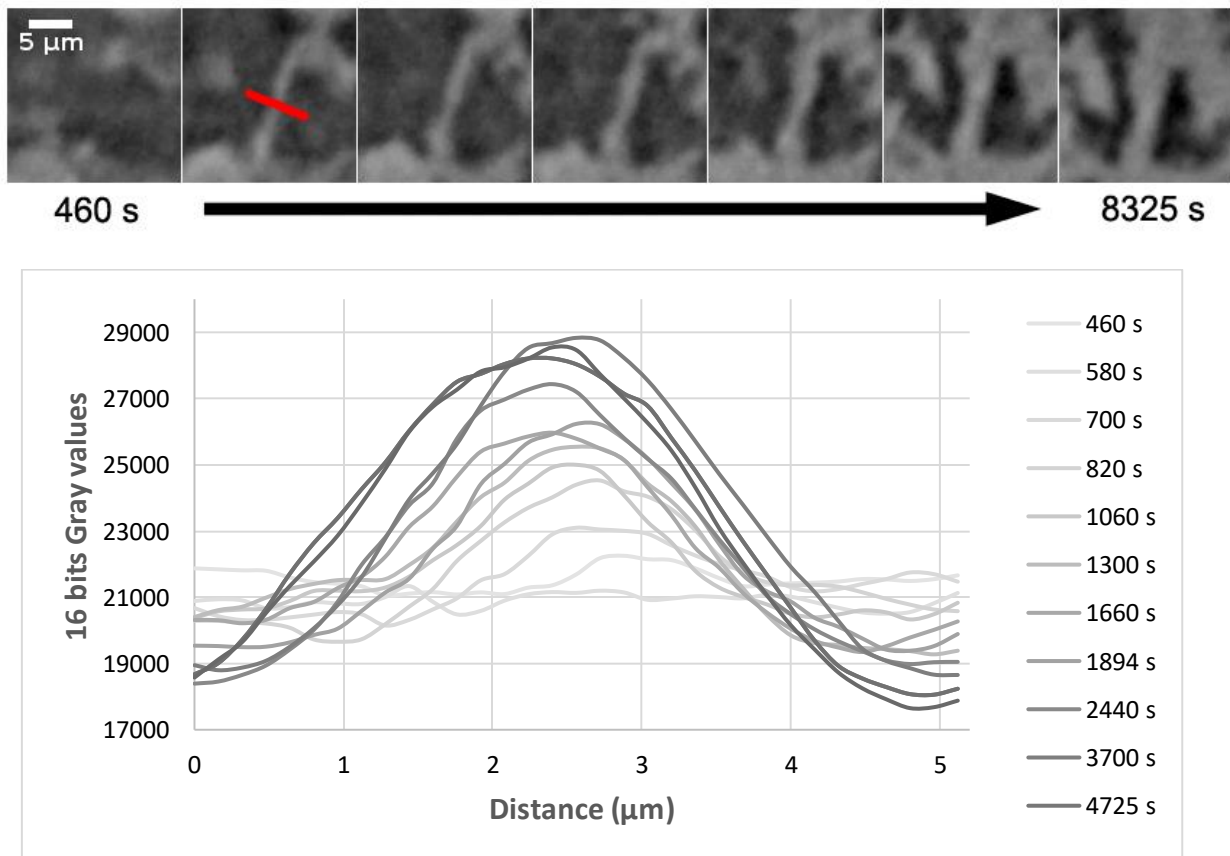


Figure 10: Top: Evolution versus time of the same 2D reconstructed slice showing the growth of a gypsum crystal, voxel size 0.163 μm . Bottom: gray level profiles across the forming gypsum crystal for different times. A small offset in distance can be observed for the two last curves at 6561 s and 8325 s as the stabilization of the images with time could not be performed perfectly.

Second, a total of seven growing dihydrate crystals were isolated and their mean thicknesses (i.e. the smallest lateral dimension) were computed versus time after volume binarization using threshold 2 in Table 1 (Figure 11). It can clearly be seen that crystals keep thickening until approx. 3000 s after which they reach a final thickness of about 4 μm . Indeed, two different regimes in the thickening step can be observed: a first one, when precipitation occurs fastest until approximately 1000 s and a second one, when the precipitation rate slows down until a plateau is reached at about 3000 s. Precipitation rate was computed from two linear fits on the two regions of the curve in a similar manner as previously done for dissolution rate (Table 3). The results show a precipitation rate of 0.085 $\mu\text{m}/\text{min}$ until 1000 s and a rate of 0.036 $\mu\text{m}/\text{min}$ from 1000 to 2500 s.

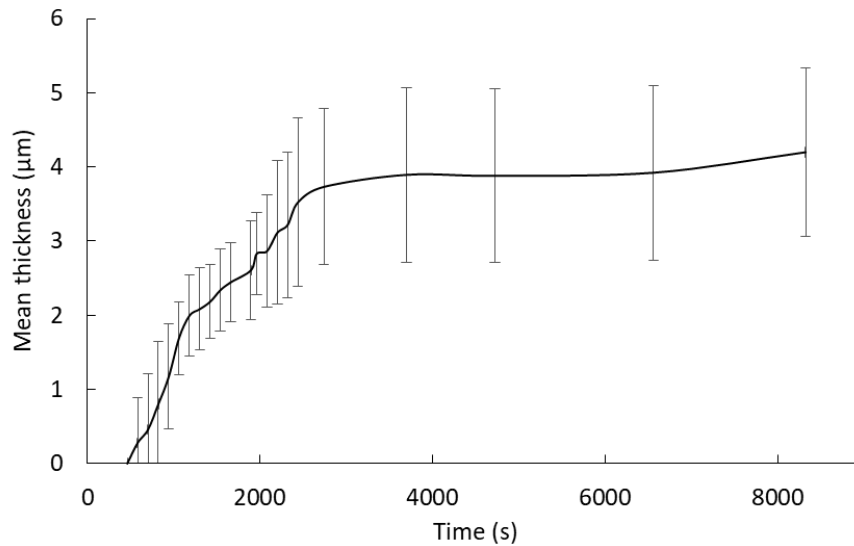


Figure 11: Evolution of gypsum crystals thickness during setting, based on an average of seven individual measures; error bars correspond to standard deviations.

4. Discussion

Qualitative and quantitative 3D analysis on reconstructed volumes permit to observe and to characterize the evolution of the microstructure of α plaster during its hydration. Due to the time required to prepare the sample and to perform the first acquisition, plaster setting could be monitored by X-ray tomography starting from a time of ~ 500 s with a voxel size of 0.65 μm and from a time of 460 s for the scan with a voxel size of 0.163 μm . *In situ* monitoring of gypsum hydration at such resolution is presented here for the first time. Provided the size of the field of view of the detector used, our analysis is performed on a small spatial region of the sample and not on its entirety, and the observed region is even smaller when very high resolution is used. This

region is located close to the middle of the recipient, so we believe that there is no effect of the edge of the cell on our observation. The small size of the observed region raises questions about the representativity and especially of our quantitative results. The size of the needles is much smaller than the field of view so our volume element can be assumed to be representative in this respect but we cannot exclude that the results in a different location would be exactly quantitatively similar.

As shown by X-ray tomography, dissolution of hemihydrate particles and precipitation of gypsum crystals in the surrounding ionic solution occurs simultaneously (Figure 2 and Figure 3). Both hemihydrate dissolution and gypsum precipitation are completed after 3000 s (Figure 8 and Figure 9 for hemihydrate dissolution and Figure 11 for gypsum precipitation), in coherence with literature for α plaster [2].

For particles with initial thicknesses below 15 μm , dissolution occurs at the solid/liquid interface and leads to the displacement of this interface at a constant speed of $\sim 0.2 \mu\text{m}/\text{min}$. The characterization of the dissolution rate is possible on volumes acquired at 0.65 μm on larger particles, even if less precise. Values lying between 0.1 and 0.2 $\mu\text{m}/\text{min}$ are found. At a voxel size of 0.65 μm , the biggest hemihydrate particles are never totally dissolved probably due to water shortage in this sample, while at a voxel size of 0.163 μm largest hemihydrate particles dissolve completely and leave place to mesopores.

In a previous work on the monitoring of plaster hydration using a laboratory X-ray tomograph, the dissolution rate of β hemihydrate particles was found to increase with increasing particle thicknesses. For particles below 10 μm in thickness (the smallest characterized in our previous work), dissolution was of 0.24 $\mu\text{m}/\text{min}$ close to the value of this work [18].

The densification of the solid matrix with time, related to gypsum precipitation, is supported by a small shift of the peak associated with gypsum crystals to higher gray values during setting. This can be explained by the spatial resolution, which even if largely improved by a synchrotron beam still affects the results for small crystals with thickness below 1 μm .

The high spatial resolution reached with the synchrotron beam permits to observe the precipitation and the growth of individual gypsum crystals. In this study both needle-shaped and lamella-shaped crystals are observed. 3D rendering of a single growing gypsum crystal shows first the formation of a thin sheet of dihydrate linking two hemihydrate particles as early as 1000 s after

mixing hemihydrate with water (Figure 10). The growth of the platelet then stops, probably due to steric effects in the entanglement of gypsum crystals. At longer times, a thickening of the crystal is observed leading to a lamella of approximately 5 μm of final thickness.

A quantitative 3D analysis on the whole acquired volume could be performed to estimate the degree of hydration at different times, using the gray level histograms. Each phase in the material shows a specific gray value, enabling the calculation of its volume fraction and therefore of a microstructural degree of hydration. In this work, a specific deconvolution procedure is developed to determine the degree of reaction as the gray values of hemihydrate and gypsum peaks are very close to each other. This is a strong improvement as compared to the method used in a previous work, consisting in the count of the number of voxels associated to the mean gray value of a given phase [18]. The evolution of volume fraction of dissolving hemihydrate, precipitating gypsum and interstitial water during setting could be calculated. The final microporosity between gypsum crystals, originating from the drying of interstitial water, was measured after 24h of drying close to the theoretical value of 29.5% (Table 1). However, in the local volume where the setting was monitored *in situ* (as illustrated in Figure 3), microporosity was estimated close to 10% in the volume scanned at 8325 s (Figure 7b). Apart from the acquisition conditions that were improved for data in Table 1 (scan after 24 hours on a dry sample without acquisition duration constrain), this difference in porosity may originate from local variations in the W/P ratio of the plaster slurry during sample preparation. Indeed, the injection of plaster slurry with a syringe into a straw does not allow for a good control of the mixing conditions, eventually leading to variation in the local W/P ratio. Variation in the local density have already been noted in cement-based materials, attributed to the relative local movement of sand and cement particles and referred to as microbleeding [28]. The influence of the irradiation of the scanned volume during hydration may also lead to an early drying and a lower local W/P in the volume considered for the *in situ* monitoring. This eventually results to uncomplete hydration as evidenced by the presence of hemihydrate particles even after the longest acquisition times. For this volume scanned after 8325 s and considering a rate of hydration of 63% and a W/P ratio of 0.18, a simple calculation based on the hydration reaction leads to 62%, 28% and 12% for gypsum, hemihydrate and porosity of respectively, similarly to the volume fractions shown in figure 7b for long hydration times.

Knife setting time was determined to be about 420 s after mixing with water, which means that early mechanical strength was already reached before the acquisition of the first scan. However, in the most rapid acquisition at 460 s, the origin of this mechanical strength could not be physically observed. Dry laser diffraction granulometry measurements confirmed the presence of very small hemihydrate particles in the initial powder (Figure 1). It can be hypothesized that those small particles dissolve almost instantly when put in contact with water and lead to the precipitation of very thin gypsum crystals, which cannot be observed by X-Ray tomography in the conditions of this work [15]. The network of crystals formed is associated to the early setting of the mix as measured by the knife test. The concentration of the ionic solution after the dissolution of the smallest hemihydrate particles (peak centered around 0.55 μm in the particle size distribution curve, Figure 1) can be estimated. As the smallest particles account for about 15.5% of the total volume of hemihydrate powder, their dissolution can lead to a maximum concentration of calcium and sulfate ions in the ionic solution of 388 g/L. This concentration is way above the maximum solubility for gypsum which is about 2.4 g/L at 20 °C [2], so it is concluded that the sole dissolution of the smallest hemihydrate particles could already lead to gypsum precipitation and thus provide an initial strength to an early entangled network of gypsum crystals.

It can be assumed that dissolution of smallest hemihydrate particles first contributes to form an initial network of dihydrate crystals and then the dissolution of largest hemihydrate particles lead to an additional precipitation and thickening of early gypsum crystals. SEM micrographs (Figure 12) confirm the presence of both crystal shapes (needles and lamellas) in the set plaster. Additionally, the rate of gypsum precipitation is found to be smaller than this of hemihydrate dissolution, which agrees with results available in literature suggesting that crystallization of dihydrate is the limiting process during hydration [29]. This conclusion stands without addition of gypsum nuclei to accelerate the reaction. In the case of gypsum seeding, commonly used industrially, the mechanisms controlling the hydration may be modified.

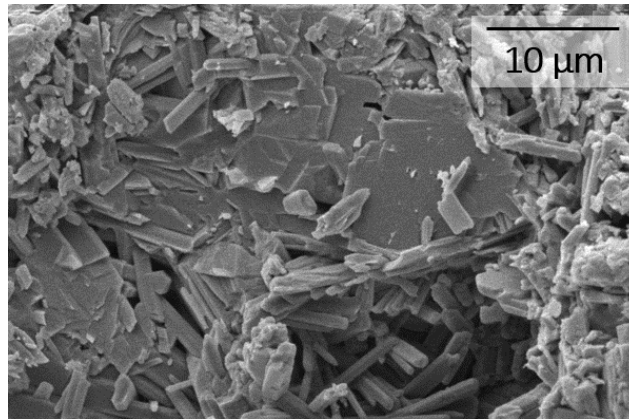


Figure 12: SEM micrograph of set alpha plaster microstructure after completed hydration.

The observed decrease in gypsum growth rate with hydration time (Figure 11) appears to be consistent with crystallization models showing hydration process as a sequence of nucleation, high growth regime and decreasing growth regime [30].

Finally, the potential impact of the synchrotron beam on the hydration reaction cannot be disregarded here. No significant difference on the temperature monitoring was noted for two similar samples subjected or not to irradiation (monitoring with a thermocouple). However changes in wettability and surface tension of water have already been reported in the literature under high brilliance synchrotron hard X-rays irradiation [31][32]. As already noted, it is possible that the high dose of the beam led to a premature local shortage of water in the sample scanned at 0.65 μm resolution for the *in situ* monitoring of the hydration, perhaps due to early evaporation of water, stopping the hydration reaction and thus preventing the biggest hemihydrate particles to dissolve totally.

5. Conclusion

In situ monitoring of α plaster setting reaction is achieved through X-ray synchrotron tomography for the first time at very high resolution (0.163 μm) and up to a quite high temporal resolution (one scan every 30 seconds).

After an incubation time, the rate of dissolution of hemihydrate particles is determined to approx. 0.2 $\mu\text{m}/\text{min}$, close to the value found for the dissolution of β hemihydrate particles of the same size in our previous work. Thanks to the use of a synchrotron line, the spatial resolution is sufficient

to quantify the precipitation rate of gypsum crystals. It appears that the gypsum crystals grow in very elongated shapes and then thicken with time, with an average rate inferior to 0.1 $\mu\text{m}/\text{min}$.

At a global scale, a microstructural degree of reaction is calculated using time evolving gray-level histograms and a specific peak deconvolution procedure, as the grey values peaks representative of gypsum and hemihydrate are overlapping. This parameter will be compared with the chemical degree of reaction in a future work.

This work also shows that rapid dissolution of very small hemihydrate particles leads to an initial precipitation of gypsum crystals, so small that they could not really be observed on the reconstructed tomograms, even at such a high resolution.

However the impact of the synchrotron beam on the dissolution kinetics should be considered as premature lack of water could be observed in one of our samples. The analysis proposed here is limited to the times for which water is still present in the material.

6. References

- [1] J. Karni, E. Karni, Gypsum in construction: origin and properties, *Mater. Struct.* 28 (1995) 92–100. <https://doi.org/10.1007/BF02473176>.
- [2] A.J. Lewry, J. Williamson, The setting of gypsum plaster - Part I The hydration of calcium sulphate hemihydrate, *J. Mater. Sci.* 29 (1994) 5279–5284. <https://doi.org/10.1007/BF01171536>.
- [3] N.B. Singh, B. Middendorf, Calcium sulphate hemihydrate hydration leading to gypsum crystallization, *Prog. Cryst. Growth Charact. Mater.* 53 (2007) 57–77. <https://doi.org/10.1016/j.pcrysgrow.2007.01.002>.
- [4] N.B. Singh, B. Middendorf, Calcium sulphate hemihydrate hydration leading to gypsum crystallization, *Prog. Cryst. Growth Charact. Mater.* 53 (2007) 57–77. <https://doi.org/10.1016/j.pcrysgrow.2007.01.002>.
- [5] L. Amathieu, R. Boistelle, Crystallization kinetics of gypsum from dense suspension of hemihydrate in water, *J. Cryst. Growth.* 88 (1988) 183–192. [https://doi.org/10.1016/0022-0248\(88\)90275-8](https://doi.org/10.1016/0022-0248(88)90275-8).
- [6] C. Solberg, S. Hansen, Dissolution of $\text{CaSO}_4 \cdot \frac{1}{2}\text{H}_2\text{O}$ and precipitation of $\text{CaSO}_4 \cdot 2\text{H}_2\text{O}$

- 2 O A kinetic study by synchrotron X-ray powder diffraction, *Cem. Concr. Res.* 31 (2001) 641–646. [https://doi.org/10.1016/S0008-8846\(01\)00464-1](https://doi.org/10.1016/S0008-8846(01)00464-1).
- [7] K.M. Song, J. Mitchell, H. Jaffel, L.F. Gladden, Simultaneous monitoring of hydration kinetics, microstructural evolution, and surface interactions in hydrating gypsum plaster in the presence of additives, *J. Mater. Sci.* 45 (2010) 5282–5290. <https://doi.org/10.1007/s10853-010-4572-7>.
- [8] A. Czaderna, A. Kocemba, M. Kozanecki, M. Mucha, P. Mróz, The influence of cellulose derivatives on water structure in gypsum, *Constr. Build. Mater.* 160 (2018) 628–638. <https://doi.org/10.1016/j.conbuildmat.2017.11.062>.
- [9] Q.L. Yu, H.J.H. Brouwers, A.C.J. de Korte, Gypsum hydration: a theoretical and experimental study, in: *17th Int. Conf. Build. Mater. Ibausil, 2009*: p. 6. <http://doc.utwente.nl/67946/>.
- [10] A.J. Lewry, J. Williamson, The setting of gypsum plaster - Part II The development of microstructure and strength, *J. Mater. Sci.* 29 (1994) 5524–5528. <https://doi.org/10.1007/BF00349943>.
- [11] P. Reynaud, M. Saâdaoui, S. Meille, G. Fantozzi, Water effect on internal friction of set plaster, *Mater. Sci. Eng. A.* 442 (2006). <https://doi.org/10.1016/j.msea.2006.01.152>.
- [12] M. Saâdaoui, S. Meille, P. Reynaud, G. Fantozzi, Internal friction study of the influence of humidity on set plaster, *J. Eur. Ceram. Soc.* 25 (2005). <https://doi.org/10.1016/j.jeurceramsoc.2004.07.035>.
- [13] S. Meille, E.J. Garboczi, Linear elastic properties of 2D and 3D models of porous materials made from elongated objects, *Model. Simul. Mater. Sci. Eng.* 9 (2001) 371–390. <https://doi.org/10.1088/0965-0393/9/5/303>.
- [14] M.J. Ridge, Effect of temperature on the structure of set gypsum plaster, *Nature.* 182 (1958) 1224–1225. <https://doi.org/10.1038/1821224a0>.
- [15] C. Liu, J. Gao, Y. Tang, Y. Zhao, Early hydration and microstructure of gypsum plaster revealed by environment scanning electron microscope, *Mater. Lett.* 234 (2019) 49–52. <https://doi.org/10.1016/j.matlet.2018.09.071>.
- [16] U. Tritschler, M. Kellermeier, C. Debus, A. Kempter, H. Cölfen, A simple strategy for the

- synthesis of well-defined bassanite nanorods, *CrystEngComm*. 17 (2015) 3772–3776. <https://doi.org/10.1039/c5ce00519a>.
- [17] D.P. Bentz, S. Mizell, S. Satterfield, J. Devaney, W. George, P. Ketcham, J. Graham, J. Porterfield, D. Quenard, F. Vallee, H. Sallee, E. Boller, J. Baruchel, The Visible Cement Data Set, *J. Res. Natl. Inst. Stand. Technol.* 107 (2002) 137. <https://doi.org/10.6028/jres.107.013>.
- [18] J. Adrien, S. Meille, S. Tadier, E. Maire, L. Sasaki, In-situ X-ray tomographic monitoring of gypsum plaster setting, *Cem. Concr. Res.* 82 (2016). <https://doi.org/10.1016/j.cemconres.2015.12.011>.
- [19] E. Maire, C. Le Bourlot, J. Adrien, A. Mortensen, R. Mokso, 20 Hz X-ray tomography during an in situ tensile test, *Int. J. Fract.* 200 (2016) 3–12. <https://doi.org/10.1007/s10704-016-0077-y>.
- [20] F. García-Moreno, P.H. Kamm, T.R. Neu, F. Bülk, R. Mokso, C.M. Schlepütz, M. Stampanoni, J. Banhart, Using X-ray tomography to explore the dynamics of foaming metal, *Nat. Commun.* 10 (2019). <https://doi.org/10.1038/s41467-019-11521-1>.
- [21] J. Villanova, R. Daudin, P. Lhuissier, D. Jauffrès, S. Lou, C.L. Martin, S. Labouré, R. Tucoulou, G. Martínez-Criado, L. Salvo, Fast in situ 3D nanoimaging: a new tool for dynamic characterization in materials science, *Mater. Today*. 20 (2017) 354–359. <https://doi.org/10.1016/j.mattod.2017.06.001>.
- [22] S. Brisard, M. Serdar, P.J.M. Monteiro, Multiscale X-ray tomography of cementitious materials: A review, *Cem. Concr. Res.* 128 (2020). <https://doi.org/10.1016/j.cemconres.2019.105824>.
- [23] E. Maire, P.J. Withers, Quantitative X-ray tomography, *Int. Mater. Rev.* 59 (2014) 1–43. <https://doi.org/10.1179/1743280413Y.0000000023>.
- [24] D. Paganin, S.C. Mayo, T.E. Gureyev, P.R. Miller, S.W. Wilkins, Simultaneous phase and amplitude extraction from a single defocused image of a homogeneous object, *J. Microsc.* 206 (2002) 33–40. <https://doi.org/10.1046/j.1365-2818.2002.01010.x>.
- [25] F. Marone, M. Stampanoni, Regridding reconstruction algorithm for real-time tomographic imaging, *J. Synchrotron Radiat.* 19 (2012) 1029–1037.

- <https://doi.org/10.1107/S0909049512032864>.
- [26] M.D. Abràmoff, P.J. Magalhães, S.J. Ram, Image processing with imageJ, *Biophotonics Int.* 11 (2004) 36–41. <https://doi.org/10.1117/1.3589100>.
- [27] J. Schindelin, I. Arganda-Carreras, E. Frise, V. Kaynig, M. Longair, T. Pietzsch, S. Preibisch, C. Rueden, S. Saalfeld, B. Schmid, J.-Y. Tinevez, D.J. White, V. Hartenstein, K. Eliceiri, P. Tomancak, A. Cardona, s, *Nat. Methods.* 9 (2012) 676–82. <https://doi.org/10.1038/nmeth.2019>.
- [28] H. Ma, Z. Li, Multi-aggregate approach for modeling interfacial transition zone in concrete, *ACI Mater. J.* 111 (2014) 189–200. <https://doi.org/10.14359/51686501>.
- [29] G. Dumazer, V. Narayan, A. Smith, A. Lemarchand, Modeling gypsum crystallization on a submicrometric scale, *J. Phys. Chem. C.* 113 (2009) 1189–1195. <https://doi.org/10.1021/jp806028v>.
- [30] J.F. Georjgin, N. Maach, J. Pommay, Sulphate crystallization modelling and surface reactivity in solution, *Constr. Build. Mater.* 156 (2017) 266–276. <https://doi.org/10.1016/j.conbuildmat.2017.08.155>.
- [31] B.M. Weon, J.H. Je, Y. Hwu, G. Margaritondo, Decreased surface tension of water by hard-X-ray irradiation, *Phys. Rev. Lett.* 100 (2008). <https://doi.org/10.1103/PhysRevLett.100.217403>.
- [32] Y.B. Kwon, B.M. Weon, K.H. Won, J.H. Je, Y. Hwu, G. Margaritondo, X-ray-induced changes in wettability, *Langmuir.* 25 (2009) 1927–1929. <https://doi.org/10.1021/la804081k>.